Low electronic conductivity of $Li_7La_3Zr_2O_{12}$ solid electrolytes from first principles

Alexander G. Squires,[1,2] Daniel W. Davies,[3] Sunghyun Kim,[4] David O. Scanlon,[3,5,2]
Aron Walsh,[4,6,2] and Benjamin J. Morgan [1,2,*]

[1]*Department of Chemistry, University of Bath, Claverton Down BA2 7AY, United Kingdom*
[2]*The Faraday Institution, Quad One, Becquerel Avenue, Harwell Campus, Didcot OX11 0RA, United Kingdom*
[3]*Department of Chemistry, University College London, 20 Gordon Street, WC1H 0AJ London, United Kingdom*
[4]*Department of Materials, Imperial College London, Exhibition Road, London SW7 2AZ, United Kingdom*
[5]*Diamond Light Source Ltd., Diamond House, Harwell Science and Innovation Campus, Didcot, Oxfordshire OX11 0DE, United Kingdom*
[6]*Department of Materials Science and Engineering, Yonsei University, Seoul 03722, Korea*

Lithium-rich garnets such as $Li_7La_3Zr_2O_{12}$ (LLZO) are promising solid electrolytes with potential application in all-solid-state batteries that use lithium-metal anodes. The practical use of garnet electrolytes is limited by pervasive lithium-dendrite growth, which leads to short-circuiting and cell failure. One proposed mechanism of lithium-dendrite growth is the direct reduction of lithium ions to lithium metal within the electrolyte, and lithium garnets have been suggested to be particularly susceptible to this dendrite-growth mechanism due to high electronic conductivities relative to other solid electrolytes. The electronic conductivities of LLZO and other lithium-garnet solid electrolytes, however, are not yet well characterized. Here, we present a general scheme for calculating the intrinsic electronic conductivity of a nominally insulating material under variable synthesis conditions from first principles, and apply this to the prototypical lithium-garnet LLZO. Our model predicts that under typical battery operating conditions, electron and hole mobilities are low (<1 cm^2 V^{-1}s^{-1}), and bulk electron and hole carrier concentrations are negligible, irrespective of initial synthesis conditions or dopant levels. These results suggest that the bulk electronic conductivity of LLZO is not sufficiently high to cause bulk lithium-dendrite growth during cell operation, and that any non-negligible electronic conductivity in lithium garnet samples is likely due to extended defects or surface contributions.

I. INTRODUCTION

All-solid-state batteries that combine a solid electrolyte with a lithium-metal anode offer the potential for significantly increased energy densities compared to conventional lithium-ion batteries [1]. The development of practical solid-state batteries requires reliable solid-state electrolytes with optimized material properties [2]. The principal requirement for a practical solid electrolyte is a high ionic conductivity. As a consequence, significant research effort has been invested in developing an understanding of the physical principles that govern fast-ion transport [3–9] and in discovering new highly conducting solid electrolytes [10–13]. In addition to a high ionic conductivity, other material properties are also necessary for a practical solid electrolyte; these include good electrochemical stability over a wide operating voltage window [14], sufficient mechanical strength to impede dendrite growth [15], and low interfacial and grain boundary resistivities [2,16]. The

development of practical solid electrolytes for use in all-solid-state batteries therefore requires a clear understanding of a broad range of relevant material properties in individual candidate materials, and how these properties may be controlled by tuning synthesis conditions or through targeted chemical modification [17–19].

One key property that can affect solid electrolyte performance is *electronic* conductivity. An ideal solid electrolyte should have minimal electronic conductivity to avoid gradual self-discharge [20,21]. A non-negligible electronic conductivity has also been suggested as a possible contributing factor for lithium dendrite growth, whereby mobile Li$^+$ ions are directly reduced to Li^0 metal within the solid-electrolyte bulk [22–25]. A recent experimental study by Han *et al.* showed that this "bulk" dendrite growth is more prevalent in solid electrolytes with high electronic conductivities [24], prompting the suggestion that electronic conductivity might be a critical parameter that determines the degree to which a given solid electrolyte is susceptible to bulk dendrite nucleation and growth. On this basis, Han *et al.* proposed empirical upper-limit thresholds for total electronic conductivity for a solid electrolyte to resist dendrite growth via bulk nucleation, of 10^{-10} and 10^{-12} S cm^{-1} at current densities of 1 and 10 mA cm^2, respectively [24].

Despite the potential impact of nonzero electronic conductivities on the use of solid electrolytes in all-solid-state

*b.j.morgan@bath.ac.uk

batteries—particularly in cells that use lithium-metal anodes—a detailed characterization of solid electrolyte electronic conductivities, and their dependence on parameters such as synthesis conditions and sample stoichiometry, is lacking for many materials. Experimental measurements of electronic conductivities are usually performed on polycrystalline samples, and non-negligible electronic conductivity values are typically attributed to contributions from grain boundaries or surfaces [23,26], with any residual bulk contributions considered to be negligible. While it may be the case that for many solid electrolytes their macroscopic electronic conductivities are dominated by *extrinsic* contributions, i.e., those arising from conductivity at surfaces and grain boundaries, it is also important to characterise the *intrinsic* bulk electronic conductivities of solid electrolytes. For example, even if the bulk electronic conductivity is small with respect to surface and grain boundary contributions, this bulk value provides a lower limit to the net macroscopic electronic conductivity that might be obtained even under optimal morphological control, e.g., after sintering or surface treatments. Solid electrolytes with bulk electronic conductivities that are higher than the threshold values proposed by Han *et al.* may be fundamentally incompatible with lithium metal anodes because they are inherently susceptible to internal dendrite nucleation, irrespective of any subsequent processing [27].

The direct experimental measurement of solid electrolyte bulk electronic conductivities can be technically challenging, and has been reported for only a few cases [21]. Bulk electronic conductivities can alternatively be calculated entirely from first principles, using schemes based on electronic structure methods. These computational models are parametrized in terms of the net stoichiometry and structure of the material and the relevant thermodynamic conditions, i.e., elemental chemical potentials and temperature. First-principles models can therefore be used to characterise how bulk electronic conductivities vary as a function of experimental variables such as synthesis conditions or extrinsic dopant concentrations, which in turn can give inform the design of optimised experimental synthesis protocols that might minimise residual electronic conductivity and limit its impact on electrolyte performance.

The electronic conductivity of a semiconductor, such as a solid electrolyte, can be calculated from the products of the concentrations and mobilities of free electrons and holes, with each determined under relevant operating conditions [28]. First-principles models for calculating carrier concentrations in semiconductors under thermodynamic equilibrium are well established [29,30], and have previously been applied to a range of battery materials [27,31–35]. Electronic carrier mobilities for semiconductors can also be calculated from first principles; using either highly accurate but computationally costly density-functional perturbation-theory methods [36–38] or more tractable schemes that introduce some level of approximation [39,40]. These latter methods, when combined with standard methods for calculating carrier concentrations, make it practical to calculate electronic conductivities of nominally insulating semiconductors, such as solid electrolytes, entirely from first principles.

Here, we describe one such computational workflow for a fully first-principles calculation of the bulk electronic con-

ductivity of a solid electrolyte, and demonstrate its use in calculating the electronic conductivity of the prototypical lithium garnet solid electrolyte tetragonal $Li_7La_3Zr_2O_{12}$ (LLZO), as a function of synthesis conditions and the degree of aliovalent (supervalent) doping. We find that electrons and holes in LLZO have low mobilities (<1 cm^2 V^{-1}s^{-1}) and electronic carrier populations are vanishingly small in undoped and doped samples under standard operating conditions. These results suggest that the bulk electronic conductivity of LLZO is not sufficiently high to cause lithium-dendrite formation during cell operation by direct reduction of lithium ions to lithium metal within the bulk material. We therefore conclude that non-negligible electronic conductivities measured in experimental lithium garnet samples, and any associated potential for dendrite nucleation and growth, are likely due to contributions from extended defects or surfaces, and that morphological control is critical to limit lithium dendrite growth due to electronic conductivity.

II. THEORY

The electronic conductivity, σ, of a semiconductor is given by

$$\sigma = n_0 q \mu_{\mathrm{n}} + p_0 q \mu_{\mathrm{p}}, \tag{1}$$

where n_0 and p_0 are the concentrations of free electrons and holes respectively, q is the magnitude of charge of each carrier species, and μ_{n} and μ_{p} are the electron and hole mobilities. For wide-gap materials, such as solid electrolytes, the thermal energy at room temperature is insufficient to generate free carriers by directly exciting electrons from the valence band to the conduction band. The presence of point defects, however, can produce free charge carriers that then participate in electronic transport [41,42]. Point defects exist even in nominally stoichiometric samples due to configurational entropy, and can also be introduced via deliberate or inadvertent doping with extrinsic species [35,43,44]. Aliovalent doping of solid electrolytes is a common synthesis strategy to increase ionic conductivities through modulation of the number of ionic charge carriers [45–47]. A secondary effect of aliovalent doping is to shift the position of the Fermi energy within the band gap. Moving the Fermi energy closer to the conduction-band or valence-band edges increases the number of thermally generated electrons or holes, respectively. Under some synthesis conditions and doping protocols the Fermi energy may move close enough to either the valence- or conduction-band edge so that the population of thermally generated electronic charge carriers is sufficiently high to give a non-negligible electronic conductivity.

Electron and hole carrier concentrations can be calculated as functions of the Fermi energy, E_{F}, and the bulk electronic density of states, $g(E)$:

$$n_0 = \int_{E_{\mathrm{CBM}}}^{\infty} \frac{1}{\mathrm{e}^{(E-E_{\mathrm{F}})/k_{\mathrm{B}}T} + 1} g(E) \, dE, \tag{2}$$

$$p_0 = \int_{-\infty}^{E_{\mathrm{VBM}}} \left(1 - \frac{1}{\mathrm{e}^{(E-E_{\mathrm{F}})/k_{\mathrm{B}}T} + 1}\right) g(E) \, dE, \tag{3}$$
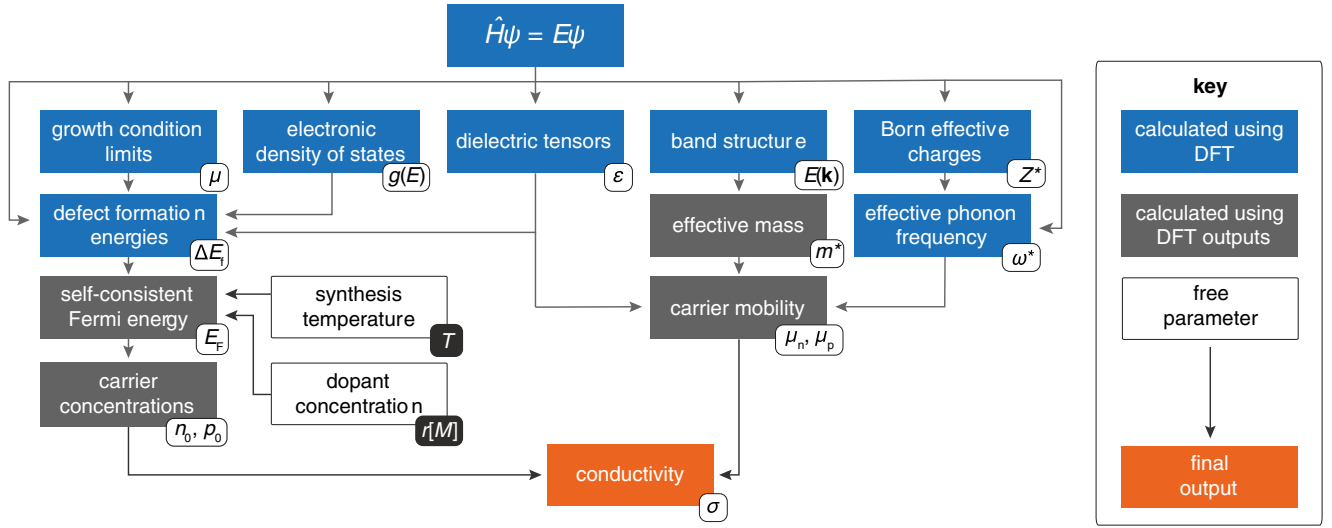
FIG. 1. Schematic showing the workflow used to calculate the electronic conductivity from first-principles inputs.

where k_B is the Boltzmann constant [48]. Point defect concentrations are given by

$$[X^q] = N_0^X \exp\left(-\frac{\Delta E_f^{X,q}[E_F, \Delta\mu_i]}{k_B T}\right), \qquad (4)$$

where N_0^X is the density of available sites for defect X, $\Delta E_f^{X,q}$ is the formation energy of defect X in charge state q, which itself depends on the Fermi energy, E_F, and $\Delta\mu_i$ are the chemical potentials of any atomic species added to or removed from the system when forming each defect [28,49]. Equations (2), (3), and (4) are coupled by a common Fermi energy, which is constrained by the requirement that the system is net charge neutral; the charge-density contributions from electrons, holes, and any charged point-defects must sum to zero:

$$\rho(E_F) = \sum_{X^q} q[X^q] + p_0 - n_0 = 0. \qquad (5)$$

Calculating equilibrium carrier concentrations under specific synthesis conditions consists of finding a self-consistent solution to Eqs. (2), (3), and (4), subject to the charge-neutrality constraint expressed in Eq. (5) [28,30].

The effect of extrinsic doping can be accounted for by including an additional term in Eq. (5) [30,35,44]. For a dopant M with relative charge r and fixed concentration $[M^r]$, ρ becomes

$$\rho(E_F, r[M^r]) = \sum_{X^q} q[X^q] + p_0 - n_0 + r[M^r]. \qquad (6)$$

In the dilute-defect limit there is no direct interaction between dopants and native defects, and the doping response does not depend on the choice of dopant species or insertion site, but only on the product $r[M^r]$ [35,44].

The necessary inputs to solve Eqs. (2)–(6) are the reference elemental chemical potentials, which are restricted by the condition that the host material must be thermodynamically stable with respect to competing phases; the native defect formation energies; the dielectric tensor for the material; and

the electronic density of states for the nondefective system. These parameters can all be obtained using first-principles methods such as density functional theory (DFT) [29,50] (Fig. 1).

For materials in which electronic charge-carriers exist as large polarons, i.e., with a polaron radius that is much larger than a typical lattice spacing [51], the electron and hole carrier mobilities—μ_n and μ_p, respectively—can be calculated using the Feynman variational solution for Fröhlich's polaron Hamiltonian and integrating the polaron-response function [52,53]. This continuum model is parametrized by the electronic carrier effective masses, the dielectric response of the material, and the harmonic phonon frequencies; the details of the crystal structure appear implicitly through these parameters, each of which can be calculated directly from specific DFT calculations (Fig. 1; full details are given in the Supplemental Material, Sec. S2 [54]). This approach to calculating carrier mobilities assumes that the polaron mobility is limited by scattering by optical phonon modes, which is the dominant factor for heteropolar crystals [55]. In real materials other scattering processes may be non-negligible [56]. Solving Fröhlich's polaron Hamiltonian therefore gives an upper limit value for the carrier mobilities in a perfect crystal.

III. CHOICE OF MODEL

We now turn to the application of the scheme described in Sec. II to calculate the bulk electronic conductivity of the lithium-ion solid electrolyte $Li_7La_3Zr_2O_{12}$ (LLZO) as a function of synthesis conditions and varied doping protocols. $Li_7La_3Zr_2O_{12}$ exhibits two phases: a low temperature tetragonal phase (t-LLZO) below $\sim$600 K, and a high-temperature cubic phase (c-LLZO). The ionic conductivity of the tetragonal phase ($\sigma \approx 10^{-6}$ S cm^{-1}) is significantly lower than that of the cubic phase ($\sigma \approx 10^{-4}$ S cm^{-1}) [57], making the cubic phase the desired form for use in all-solid-state lithium-ion batteries, and the cubic phase is usually stabilized through aliovalent doping for practical use [46].

c-LLZO and t-LLZO are structurally very similar [58,59]. These two phases have topologically identical host frameworks (i.e., excluding the lithium substructure) and the tetragonal distortion in t-LLZO is small (<4 %) [60]. The structures of c-LLZO and t-LLZO do, however, differ significantly with respect to the arrangement of lithium ions [46,58,59]. In t-LLZO the lithium ions are crystallographically ordered, and this ordering the reason for the low ionic conductivity of this phase [3]. In c-LLZO, in contrast, the lithium ions are disordered over the available lithium sites.

Our scheme for calculating the bulk electronic conductivity involves the accurate calculation of point defect concentrations, via Eq. (4). This presents a challenge for highly disordered systems because Eq. (4) is formally valid only for systems with a well-defined ordered ground state [35]. Rather than assuming that Eq. (4) approximately holds for an inherently disordered system, thereby introducing unquantified errors into our computational scheme, we instead consider here the low-temperature lithium-ordered t-LLZO phase, under the expectation that the electronic conductivity we obtain is also a reasonable estimate for conductivity of the high-temperature c-LLZO phase.

Our expectation that results obtained for t-LLZO are also approximately valid for c-LLZO is based on the close structural and electronic similarity between these two phases. As already noted, the only significant structural difference between t-LLZO and c-LLZO is the degree to which lithium ions are ordered versus disordered. Because lithium does not contribute strongly to the valence band or conduction band edge states (see Supplemental Material, Fig. S1 [54]), differences in the lithium substructure are not expected to significantly affect electron or hole carrier mobilities. This assumption is supported by calculated electron and hole effective masses for t-LLZO and c-LLZO using the PBEsol functional (Supplemental Material, Sec. S1 [54]), which differ by only 14 % and 60 %, respectively; electronic carrier mobilities in t-LLZO and c-LLZO are predicted to be the same to within one order of magnitude. The degree to which lithium is ordered or disordered is also not expected to significantly affect the concentrations of the electronic charge carriers. Lithium disorder in c-LLZO can formally be described in terms of Frenkel pairs that comprise equal numbers of lithium "interstitials" and "vacancies" and are net charge neutral. Changes in lithium substructure therefore cannot significantly shift the Fermi energy position. Hence, for identical synthesis and doping protocols, t-LLZO and c-LLZO will exhibit similar concentrations of electron and hole charge carriers.

Our scheme for calculating electron and hole mobilities uses the Feynman variational solution for Fröhlich's polaron Hamiltonian, which is appropriate in the large polaron regime, where the characteristic polaron radius is much larger than a typical lattice spacing. Solving the Fröhlich polaron model using DFT-derived parameters for t-LLZO (for full details see the Supplemental Material, Sec. S2 [54]) gives an effective polaron radius of > 30 Å. This extends well beyond the t-LLZO unit-cell length of ~ 13 Å, supporting our assumption that carriers in LLZO can be modeled as large polarons. As a further test for whether small polarons form in LLZO, we performed an additional hybrid DFT calculation on the 96 atom t-LLZO primitive cell with one "excess" electron
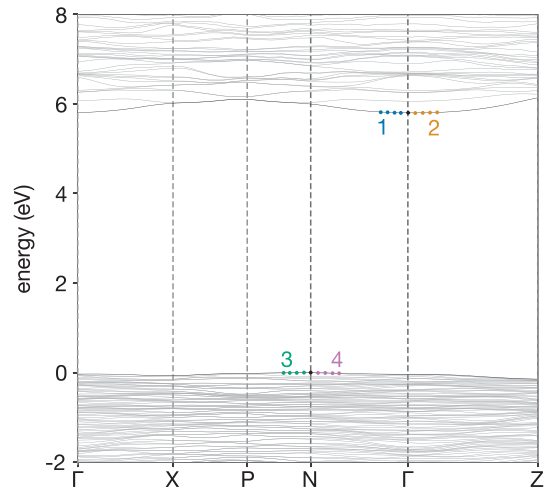

FIG. 2. The electronic band structure of t-LLZO calculated using HSE06, plotted along a high symmetry path in the Brillouin zone according to the Bradley and Cracknell notation [91]. The colored points mark the band edges used to calculate the effective masses, with numeric labels indicating the corresponding entry in Table I.

added (Supplemental Material, Sec. S2 [54]). The electronic structure obtained from this calculation is consistent with the formation of large polarons, in agreement with the calculated polaron radius obtained from the Fröhlich polaron model. The excess charge associated with the additional electron occupies a delocalised state at the bottom of the conduction band, rather than a narrow mid-gap state that would typically be associated with small polaron formation (Supplemental Material, Fig. S3 [54]). We also observe no spontaneous localization of the excess charge density on individual La or Zr sites, again suggesting electrons do not self-trap as small polarons in LLZO.

IV. COMPUTATIONAL METHODS

To parametrize our model, we have used DFT data from our previous study of the intrinsic defect chemistry of tetragonal LLZO [35], which are available as Ref. [61]. Python scripts used for all our post-DFT analysis and for plotting Figs. 2–5 are available at Ref. [62]. The DFT dataset we use is available at Ref. [63]. Our analysis relies on several open-source Python packages, including PYMATGEN [64], MATPLOTLIB [65], PANDAS [66], NUMPY [67], SCIPY [68], PHONOPY-SPECTROSCOPY [69], VASPPY [70], TQDM [71], EFFMASS [72], and the Julia package POLARONMOBILITY.JL

TABLE I. Curvature effective masses, m^*, for holes and electrons determined by a parabolic fit to LLZO band edges [72], and the relevant crystallographic direction for transport. Numbers indicate the corresponding features in the electronic band structure (Fig. 2).

Carrier	Direction	m^*	No.
electron	$\Gamma \longrightarrow N$	2.35	1
electron	$\Gamma \longrightarrow Z$	2.41	2
hole	$N \longrightarrow P$	2.39	3
hole	$N \longrightarrow \Gamma$	21.44	4

[39,73]. The code used to model defect and carrier concentrations is a Python reimplementation of the Fortran code SC-FERMI [30], and is available at Ref. [74].

All DFT data used in this study have been computed using the plane-wave DFT code VASP [75–77]. Interactions between core and valence electrons are described using pseudopotentials within the projector-augmented wave (PAW) method [78]. Unless otherwise noted, all calculations used the hybrid-DFT functional HSE06 [79,80] and a plane-wave cutoff of 520 eV. Optimized lattice parameters were obtained by performing a series of constant-volume geometry optimization calculations, and fitting the resulting energy-volume data to the Murnaghan equation of state [81]. k-point sampling was selected to ensure energies converged to < 1 meV/atom: all LLZO calculations used a $2\times2\times2$ Monkhorst-Pack k-point mesh. k-point sampling for competing phases and elemental reference calculations is described in the supporting dataset [63].

The high-frequency dielectric function was calculated using the method of Gajdoš *et al.* [82], while the ionic response was calculated using density functional perturbation theory using the PBEsol generalized gradient approximation (GGA) functional [83]. Effective masses were calculated from fitting to the LLZO band structure, calculated non-self-consistently using the charge density data obtained from a single-point electronic-structure calculation following geometry optimization.

To calculate defect formation energies, we use the supercell approach [29,50]. The defects considered in our study are lithium vacancies and interstitials, V_{Li} and Li_i; oxygen vacancies and interstitials, V_O and O_i; holes on framework oxygen, $O_O^{\bullet}$; lanthanum and zirconium vacancies, V_{La} and V_{Zr}; zirconium interstitials, Zr_i; and cation antisites La_{Zr}, Zr_{Li}^{oct}, Zr_{Li}^{tet}, Zr_{La}, Li_{La}, La_{Li}^{oct}, and Li_{Zr}. A superscript oct or tet denotes a defect located at an octahedral or tetrahedral Li site, respectively. Structural relaxations for all defects were calculated with cell parameters fixed to the optimized values for stoichiometric LLZO. Electrostatic potentials of the bulk and defective calculations were aligned via the difference in spatially averaged electrostatic potentials in the two simulation cells. We use the image charge correction scheme of Lany and Zunger [84], adapted for anisotropic systems by Murphy and Hine [85].

V. RESULTS

A. Carrier mobilities

The electronic conductivity of t-LLZO is given by the products of carrier concentrations and carrier mobilities, summed over contributions from both electron and hole carriers [Eq. (1)]. For the carrier mobilities, we are interested in the values under typical cell operating conditions, which we take as 298 K. Our model assumes that carrier mobilities do not vary with changes in synthesis conditions or doping levels. Within the considered range of synthesis conditions all low-energy defects are fully ionised, i.e., these defects are in charge states that correspond to their formal oxidation states, and therefore do not introduce any new defect states into the band gap. The carrier mobilities therefore act as fixed scaling

factors that can be used to convert carrier concentrations—which do vary according to synthesis conditions and doping levels—into electronic conductivities.

To solve Fröhlich's polaron model, we first determine the electron and hole effective masses. In conventional semiconductors such as those used as thermoelectrics [86] or transparent conducting oxides [87] carrier concentrations can be moderately high and band-filling effects must be accounted for when computing carrier effective masses [88]. Carrier populations in wide-gap insulators such as LLZO, however, are significantly lower than in conventional semiconductors, and band-filling effects are negligible; we therefore calculate *curvature* effective-masses at the conduction band minimum (CBM) and valence band maximum (VBM).

The band structure for t-LLZO is shown in Fig. 2, and the resulting effective masses are given in Table I. The lowest calculated effective mass—which corresponds to the highest mobility carrier—at either the CBM or VBM is 2.35 m_e [89]. Using these data to calculate room-temperature carrier mobilities, via the Feynman variational solution for Fröhlich's polaron Hamiltonian, yields a maximum value—considering both electron and hole mobilities—of 0.2 cm^2 V^{-1} s [90].

B. Carrier concentrations

Electron and hole carrier populations are given by Eqs. (2) and (3), which are solved self-consistently along with Eq. (4), which describes point-defect concentrations, under the constraint of net charge neutrality [Eqs. (5) or (6)] [35,44]. This self-consistent calculation requires specifying the thermodynamic conditions, i.e., defining the temperature, which appears in Eqs. (2) and (4) and the reference elemental chemical potentials, which affect the defect formation energies [Eq. (4)]. While our model treats the elemental chemical potentials as free parameters, in our analysis we restrict this chemical potential space to values that are, in principle, experimentally accessible; we consider only sets of chemical potentials where LLZO is thermodynamically stable with respect to competing phases [35,92]. The predicted region of thermodynamic stability of LLZO spans a four-dimensional chemical-potential space, $\{\Delta\mu_{Li}, \Delta\mu_O, \Delta\mu_{La}, \Delta\mu_{Zr}\}$, that can be broadly characterized along an O-rich/metal-poor→O-poor/metal-rich axis (Fig. 3). To further restrict this region to values corresponding to typical synthesis conditions, we relate the oxygen chemical potential to the synthesis pressure, P, and temperature, T, via

$$\Delta\mu_O(T, P) = \frac{1}{2}\left\{ C_p(T - T_0) - T\left[S_0 + C_p \ln\frac{T}{T_0} + k_B \ln\frac{P}{P_0}\right]\right\}, \quad (7)$$

using the experimental value for the oxygen standard entropy, $S_0 = 205$ J mol^{-1} K^{-1} [93]. Assuming oxygen behaves as an ideal gas, we use $C_p = (7/2)k_B$ for the constant-pressure specific-heat capacity per diatomic molecule. This reproduces well experimentally tabulated values of $\Delta\mu_O(T, P)$, with a maximum error of ~15 meV at the higher end of the temperature range under which LLZO is typically synthesized (1500 K) [94,95]. The full thermodynamic-stability region of
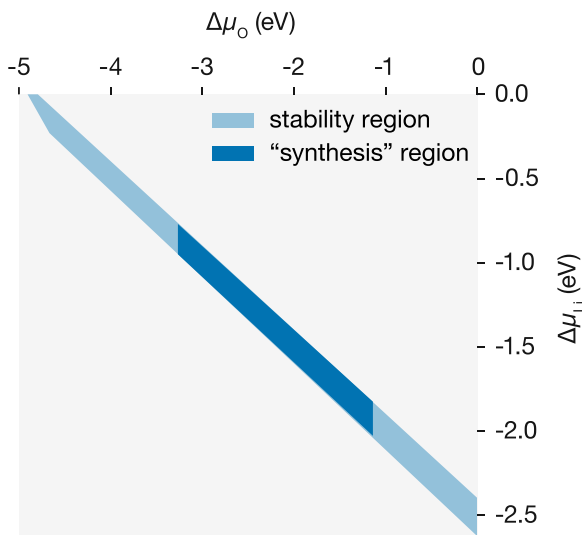
FIG. 3. Chemical potential stability region of LLZO in the $\{\Delta\mu_{Li}, \Delta\mu_O\}$ plane. The dark blue region is constricted by Eq. (7) to typical synthesis conditions ranging from $T = 1000$ to 1500 K and $P_{O_2} = 1$ to 1×10^{-10} atm.

LLZO is further limited by additional constraints that we place on the oxygen chemical potential, corresponding to synthesis temperatures of 1000 to 1500 K and oxygen partial pressures of 1 to 1×10^{-10} atm. The reduced synthetically accessible chemical potential space is plotted in the $\{\Delta\mu_{Li}, \Delta\mu_O\}$ plane in Fig. 3.

LLZO is typically synthesised at high temperature (up to 1500 K). Here, however, we are interested in predicting the electronic conductivity at much lower temperatures that correspond to typical operating conditions: approximately 298 K. We assume that host-framework point defects—those involving La, Zr, or O—formed during synthesis are "frozen in" during subsequent cooling to operating temperatures. The kinetic barriers for the reorganization of such defects within the host framework are large, which prevents the system from fully reequilibrating at low temperatures on experimentally relevant timescales [96]. Because LLZO is a fast-ion solid electrolyte with highly mobile lithium interstitials and vacancies, we do, however, expect V_{Li} and Li_i defects to reequilibrate during cooling. Electron and hole populations are similarly expected to reequilibrate on experimentally relevant timescales [34,97].

To obtain electron and hole carrier concentrations under operating conditions as a function of initial synthesis conditions, we therefore first calculate self-consistent defect and charge-carrier concentrations for the relevant range of elemental chemical potentials at a characteristic synthesis temperature of 1500 K. We then fix the concentrations of all defects except for V_{Li} and Li_i, and recompute pseudoequilibrium defect and charge-carrier populations at a range of lower temperatures, to model how the carrier concentrations change during sample cooling. For this second calculation, we impose the constraint that there is no lithium exchange with the surroundings during cooling, i.e., the net lithium stoichiometry is set by the high-temperature synthesis conditions.

To model the effect of varying synthesis conditions on the resulting carrier concentrations, we consider six chemical potential limits that correspond to the vertices of the estimated synthetically accessible chemical-potential space (Fig. 3). These six chemical-potential limits can be classified into two groups: O-rich/metal-poor or O-poor/metal-rich. The calculated pseudo-equilibrium electron and hole carrier-concentrations as a function of reequilibration temperature are plotted for each chemical-potential limit in Fig. 4. For each set of synthesis conditions we present results for undoped LLZO, where only intrinsic defects are included in the model, and for aliovalently doped LLZO, where we include a generic supervalent dopant with relative charge $r = +2$ at a concentration of 0.15 per formula unit, to model the effect of a supervalent dopant, such as Al^{3+}, occupying a lithium site, i.e., $Al_{Li}^{\bullet\bullet}$ [see Eq. (6)] [95,98,99]. The calculated defect formation energies as a function of Fermi energy for each chemical potential limit, and the calculated self-consistent Fermi energy in each case, are plotted in the Supplemental Material (Fig. S2) [54].

Under O-rich/metal-poor conditions (Fig. 4; top panels) we predict p-type conductivity at a synthesis temperature of 1500 K, with some systems becoming n-type conducting when cooled to room temperature. In contrast, under O-poor/metal-rich conditions we predict strong n-type behavior irrespective of the exact synthesis conditions. The total number of charge carriers (summing both electrons and holes) is in general slightly higher for samples synthesised under O-poor/metal-rich conditions than under O-rich/metal-poor conditions. For all synthesis conditions, and for undoped and doped samples, carrier concentrations decreases from 10^{12} / cm³ or higher at a synthesis temperature of 1500 K to a negligibly small value at room temperature ($<10^0$ / cm³). These negligible room-temperature electronic carrier concentrations are a consequence of the Fermi energy being "pinned" near the middle of the band gap for all synthesis conditions and doping specifications, by either the V'_{Li}-$Li_i^{\bullet}$ or Li'''_{Zr}-$Li_i^{\bullet}$ defect equilibria [35]. The calculated self-consistent Fermi energies are each between 2.67 and 3.78 eV above the valence band maximum, with the conduction band minimum 5.9 eV above the valence band.

C. Electronic conductivities

The results above predict that, under all considered synthesis conditions, carrier concentrations are relatively high at the initial synthesis temperature of 1500 K, but decrease by many orders of magnitude as the temperature is reduced under pseudoequilibrium conditions. The significance of this decrease in carrier concentrations can be seen by plotting approximate electronic conductivities [via Eq. (1)] which we obtain by scaling our predicted carrier concentrations by the previously calculated maximum room-temperature carrier mobility of 0.2 cm² V⁻¹s. The resulting "room-temperature" intrinsic (undoped) and extrinsic (doped) electronic conductivities are plotted in Fig. 5 for both O-rich/metal-poor and O-poor/metal-rich conditions, as a function of the pseudo re-equilibration temperature. In both cases, at a synthesis temperature of 1500 K, where the electronic carrier concentrations are high, the electronic conductivities are well in excess of the threshold values proposed by Han *et al.*
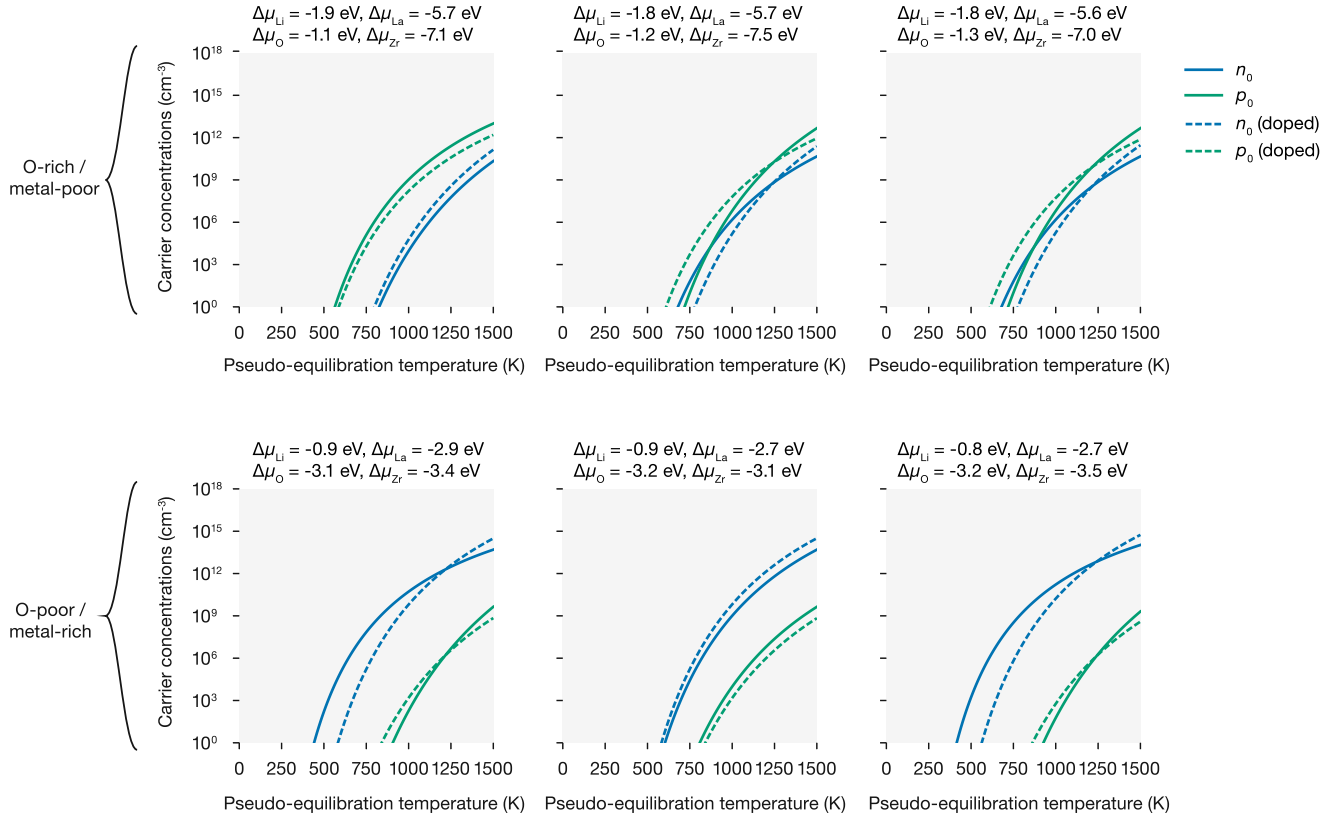
FIG. 4. n- and p-type carrier concentrations at six sets of chemical potentials (each set corresponds to a vertex of the estimated chemical potential stability region that LLZO can be synthesised within). The chemical potentials used to calculate defect concentrations are shown above each plot. The carrier concentrations are calculated at 1500 K initially, the concentrations of all defects other than lithium vacancies, interstitials and electron and hole concentrations are then fixed to these high temperature values for subsequent, lower temperature solutions. All carrier concentrations are given for both an undoped sample, and a sample containing 0.15 per formula unit of some dopant M^{2+}.

Under cooling to room temperature, however, and allowing for reequilibration of $V'_{\text{Li}}/\text{Li}^{\bullet}_{\text{i}}$ and $e^-/h^{\bullet}$ pairs, the very low predicted electronic carrier concentrations mean that the predicted room-temperature electronic conductivities are well below the threshold values proposed by Han *et al.* for intrinsic bulk lithium-dendrite growth.

VI. SUMMARY AND DISCUSSION

Minimizing the electronic conductivity of lithium solid electrolytes is crucial to the effective operation of a solid state battery. In recent years, non-negligible electronic conductivity has been linked to lithium-dendrite growth in lithium solid electrolytes, leading to cell failure [22,24]. This raises the question of whether the intrinsic electronic conductivity of various solid state electrolytes makes them fundamentally incompatible with a lithium metal anode. Motivated by this proposal, and to provide an estimate of the room-temperature bulk electronic conductivities of lithium-garnet solid electrolytes, we have presented a general fully first-principles scheme for calculating bulk electronic conductivities of wide-gap semiconductors, and have calculated the electronic conductivity of the lithium-conducting solid electrolyte LLZO, as a function of synthesis conditions and doping protocol.

We find that electronic carriers have low mobilities (<1 cm^2 V^{-1} s) owing to large hole and electron effective masses and strong electron-phonon interactions. These values are obtained by solving Fröhlich's large polaron Hamiltonian, which is appropriate in the regime of weak electron-phonon coupling and large polarons. While we cannot exclude the possibility of small polaron formation in LLZO, small polarons would be expected to have even lower mobilities [51], giving correspondingly reduced electronic conductivities. While the electronic carrier populations predicted under typical synthesis conditions ($\sim$1500 K) are sufficiently high that the corresponding room-temperature electronic conductivities would be well in excess of the threshold values proposed by Han *et al.*, these electronic carrier populations decrease significantly under subsequent sample cooling. At room temperature, assuming full reequilibration of $e^-/h^{\bullet}$ carriers (and $V_{\text{Li}}/\text{Li}_{\text{i}}$ defects), carrier concentrations are predicted to be negligible ($<10^0$ / cm^3), giving room-temperature electronic conductivities that are well below the threshold values of Han *et al.*

This prediction of very low room-temperature bulk electronic conductivity is qualitatively consistent with experimental data that gives an upper limit for the electronic conductivity of Ga-doped LLZO (Li$_{6.4}$Ga$_{0.2}$La$_3$Zr$_2$O$_{12}$) of 5×10^{-10} S cm^{-1} at 293 K [21], which is lower than macroscopic electronic conductivities reported in previous studies
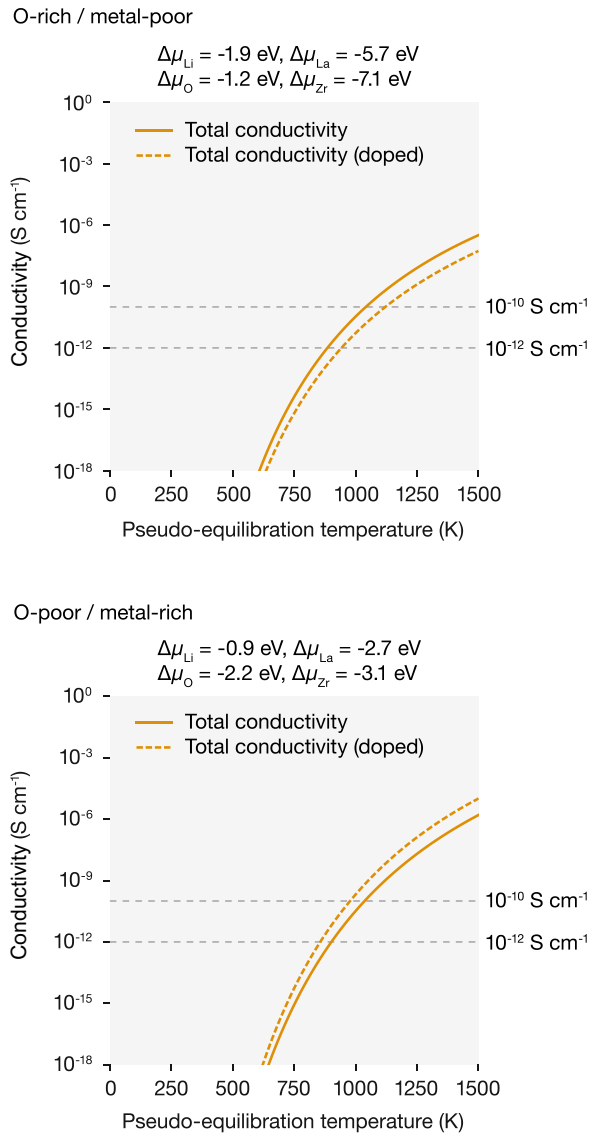
FIG. 5. Effective "room temperature" (298 K) electronic conductivities for LLZO synthesised under O-rich/metal-poor (top panel) and O-poor/metal-rich (bottom panel) conditions, as a function of $\{V_{Li}, Li_i\}$ and $\{e^-/h^\bullet\}$ pseudoequilibration temperature. Conductivities are calculated via Eq. (1), using the electronic carrier concentrations in Fig. 4 and the previously calculated maximum room-temperature electron and hole carrier mobilities of 0.2 cm^2 V^{-1}s. Solid lines show results for undoped LLZO, and dashed lines show results under supervalent doping with M^{2+} at a concentration of 0.15 per formula unit.

[24,100–102]. We note that our predicted electronic conductivities are even lower still ($<10^{-18}$ S cm^{-1}). Even within the approximations made in our model, this result suggests that the true bulk electronic conductivity of LLZO is even lower than the previously reported upper-limit value [103].

In the context of understanding the possible contribution of electronic conductivity to dendrite nucleation and growth, another limitation of the present study is that it considers only *bulk* properties. Real-world solid electrolytes possess surfaces and (usually) grain boundaries, which may contribute to net electronic conductivities or might promote lithium-dendrite growth through other mechanisms. Previous theoretical work has observed dramatic band-gap reductions at LLZO surfaces ($E_g^{bulk} = 5.46$ eV, $E_g^{surface} = 2.19$ eV) [26] and a recent combined experimental and theoretical study predicts similar narrowing at grain boundaries ($E_g^{bulk} = 6$ eV, $E_g^{gb} = 1$ eV to 3 eV) [104]. Such band-gap narrowing is expected to greatly increase the number of free charge-carriers at thermal equilibrium, potentially giving high local electronic conductivities that may facilitate dendrite nucleation and growth.

Grain boundaries and surfaces may also exhibit non-bulk defect populations. Local variations in defect standard chemical potentials can drive defect segregation to (or from) these regions, causing local shifts in the electrostatic potential (band bending) and increasing (or decreasing) local free carrier populations relative to the bulk [105]. For electrodes under applied potentials, mobile defects will also preferentially segregate to or from electrode-electrolyte interface regions to form non-charge-neutral electric-double-layer-like space-charge layers [106,107], again causing local carrier concentrations to deviate from bulk values. Extended defects such as grain boundaries may also change the local effective masses of electronic carriers: in the extreme case of very thin electrolytes, this may allow direct tunneling of electronic charge, changing the dominant electronic transport mechanism through the solid electrolyte [108]. Obviously, for a practical solid electrolyte, any such "electron leakage" is undesirable, irrespective of the question of potential lithium dendrite growth. This consideration further highlights how sample morphology can cause significant deviations from "bulk" electronic conductivities such as those we calculate here, and should be considered for a more complete model of electronic transport in solid electrolytes.

Finally, we note that lithium nucleation has been observed at grain boundaries in LLZO in recent experimental studies [23,104], which illustrates the likely critical role of sample morphology on dendrite growth in lithium garnets, and underscores the need for the development of new theoretical methods that can accurately model equilibrium defect and free carrier populations at interfaces, such as grain boundaries and surfaces.

[1] Q. Zhao, S. Stalin, C.-Z. Zhao, and L. A. Archer, Designing solid-state electrolytes for safe, energy-dense batteries, Nat. Rev. Mater. **5**, 229 (2020).

[2] T. Famprikis, P. Canepa, J. A. Dawson, M. S. Islam, and C. Masquelier, Fundamentals of inorganic solid-state electrolytes for batteries, Nat. Mater. **18**, 1278 (2019).

[3] M. Burbano, D. Carlier, F. Boucher, B. J. Morgan, and M. Salanne, Sparse Cyclic Excitations Explain the Low Ionic Conductivity of Stoichiometric $Li_7La_3Zr_2O_{12}$, Phys. Rev. Lett. **116**, 135901 (2016).

[4] X. He, Y. Zhu, and Y. Mo, Origin of fast ion diffusion in superionic conductors, Nat. Commun. **8**, 15893 (2017).

[5] M. A. Kraft, S. P. Culver, M. Calderon, F. Böcher, T. Krauskopf, A. Senyshyn, C. Dietrich, A. Zevalkink, J. Janek, and W. G. Zeier, Influence of lattice polarizability on the ionic conductivity in the lithium superionic argyrodites Li_6PS_5X ($X =$ Cl, Br, I), J. Am. Chem. Soc. **139**, 10909 (2017).

[6] D. D. Stefano, A. Miglio, K. Robeyns, Y. Filinchuk, M. Lechartier, A. Senyshyn, H. Ishida, S. Spannenberger, D. Prutsch, S. Lunghammer, D. Rettenwander, M. Wilkening, B. Roling, Y. Kato, and G. Hautier, Superionic diffusion through frustrated energy landscape, Chem **5**, 2450 (2019).

[7] S. P. Culver, A. G. Squires, N. Minafra, C. W. F. Armstrong, T. Krauskopf, F. Böcher, C. Li, B. J. Morgan, and W. G. Zeier, Evidence for a solid-electrolyte inductive effect in the superionic conductor $Li_{10}Ge_{1-x}Sn_xP_2S_{12}$, J. Am. Chem. Soc. **142**, 21210 (2020).

[8] B. J. Morgan, Mechanistic origin of superionic lithium diffusion in anion-disordered Li_6PS_5X argyrodites, Chem. Mater. **33**, 2004 (2021).

[9] B. J. Morgan, Understanding fast-ion conduction in solid electrolytes, Philos. Trans. R. Soc. A **379**, 20190451(2021).

[10] Y. Zhang, X. He, Z. Chen, Q. Bai, A. M. Nolan, C. A. Roberts, D. Banerjee, T. Matsunaga, Y. Mo, and C. Ling, Unsupervised discovery of solid-state lithium ion conductors, Nat. Commun. **10**, 5260 (2019).

[11] L. Kahle, A. Marcolongo, and N. Marzari, High-throughput computational screening for solid-state Li-ion conductors, Energy Environ. Sci. **13**, 928 (2020).

[12] S. Muy, J. Voss, R. Schlem, R. Koerver, S. J. Sedlmaier, F. Maglia, P. Lamp, W. G. Zeier, and Y. Shao-Horn, High-throughput screening of solid-state Li-ion conductors using lattice-dynamics descriptors, iScience **16**, 270 (2019).

[13] A. D. Sendek, E. D. Cubuk, E. R. Antoniuk, G. Cheon, Y. Cui, and E. J. Reed, Machine learning-assisted discovery of solid Li-ion conducting materials, Chem. Mater. **31**, 342 (2019).

[14] W. D. Richards, L. J. Miara, Y. Wang, J. C. Kim, and G. Ceder, Interface stability in solid-state batteries, Chem. Mater. **28**, 266 (2016).

[15] C. Monroe and J. Newman, The impact of elastic deformation on deposition kinetics at lithium/polymer interfaces, J. Electrochem. Soc. **152**, A396 (2005).

[16] J. Janek and W. G. Zeier, A solid future for battery development, Nat. Energy **1**, 16141 (2016).

[17] S. Ohno, T. Bernges, J. Buchheim, M. Duchardt, A.-K. Hatz, M. A. Kraft, H. Kwak, A. L. Santhosha, Z. Liu, N. Minafra, F. Tsuji, A. Sakuda, R. Schlem, S. Xiong, Z. Zhang, P. Adelhelm, H. Chen, A. Hayashi, Y. S. Jung, B. V. Lotsch *et al.*, How certain are the reported ionic conductivities

of thiophosphate-based solid electrolytes? An interlaboratory study, ACS Energy Lett. **5**, 910 (2020).

[18] S. Ohno, A. Banik, G. F. Dewald, M. A. Kraft, T. Krauskopf, N. Minafra, P. Till, M. Weiss, and W. G. Zeier, Materials design of ionic conductors for solid state batteries, Prog. Energy **2**, 022001 (2020).

[19] A. Banik, T. Famprikis, M. Ghidiu, S. Ohno, M. A. Kraft, and W. G. Zeier, On the underestimated influence of synthetic conditions in solid ionic conductors, Chem. Sci. **12**, 6238 (2021).

[20] B. V. Lotsch and J. Maier, Relevance of solid electrolytes for lithium-based batteries: A realistic view, J. Electroceram. **38**, 128 (2017).

[21] M. Philipp, B. Gadermaier, P. Posch, I. Hanzu, S. Ganschow, M. Meven, D. Rettenwander, G. J. Redhammer, and H. M. R. Wilkening, The electronic conductivity of single crystalline Ga-stabilized cubic $Li_7La_3Zr_2O_{12}$: A technologically relevant parameter for all-solid-state batteries, Adv. Mater. Interfaces **7**, 2000450 (2020).

[22] F. Aguesse, W. Manalastas, L. Buannic, J. M. Lopez del Amo, G. Singh, A. Llordés, and J. Kilner, Investigating the dendritic growth during full cell cycling of garnet electrolyte in direct contact with Li metal, ACS Appl. Mater. Interfaces **9**, 3808 (2017).

[23] Y. Song, L. Yang, W. Zhao, Z. Wang, Y. Zhao, Z. Wang, Q. Zhao, H. Liu, and F. Pan, Revealing the short-circuiting mechanism of garnet-based solid-state electrolyte, Adv. Energy Mater. **9**, 1900671 (2019).

[24] F. Han, A. S. Westover, J. Yue, X. Fan, F. Wang, M. Chi, D. N. Leonard, N. J. Dudney, H. Wang, and C. Wang, High electronic conductivity as the origin of lithium dendrite formation within solid electrolytes, Nat. Energy **4**, 187 (2019).

[25] An analogous degradation process due to reduction of Na^+ to Na resulting from electronic conduction has been discussed for Na-beta-alumina [115,116].

[26] H.-K. Tian, Z. Liu, Y. Ji, and Chen, Interfacial electronic properties dictate Li dendrite growth in solid electrolytes, Chem. Mater. **31**, 7351 (2019).

[27] P. Gorai, T. Famprikis, B. Singh, V. Stevanović, and P. Canepa, Devil is in the defects: Electronic conductivity in solid electrolytes, Chem. Mater. **33**, 7484 (2021).

[28] N. Ashcroft, *Solid State Physics* (Cengage Learning, Andover, UK, 1976)

[29] C. Freysoldt, B. Grabowski, T. Hickel, J. Neugebauer, G. Kresse, A. Janotti, and C. G. Van de Walle, First-principles calculations for point defects in solids, Rev. Mod. Phys. **86**, 253 (2014).

[30] J. Buckeridge, Equilibrium point defect and charge carrier concentrations in a material determined through calculation of the self-consistent Fermi energy, Comput. Phys. Commun. **244**, 329 (2019).

[31] M. D. Radin and D. J. Siegel, Charge transport in lithium peroxide: Relevance for rechargeable metal-air batteries, Energy Environ. Sci. **6**, 2370 (2013).

[32] J. G. Smith, J. Naruse, H. Hiramatsu, and D. J. Siegel, Intrinsic conductivity in magnesium-oxygen battery discharge products: MgO and MgO_2, Chem. Mater. **29**, 3152 (2017).

[33] H. Park, N. Kumar, M. Melander, T. Vegge, J. M. G. Lastra, and D. J. Siegel, Adiabatic and nonadiabatic charge transport in Li-S batteries, Chem. Mater. **30**, 915 (2018).

[34] P. Canepa, G. S. Gautam, D. Broberg, S.-H. Bo, and G. Ceder, Role of point defects in spinel Mg chalcogenide conductors, Chem. Mater. **29**, 9657 (2017).

[35] A. G. Squires, D. O. Scanlon, and B. J. Morgan, Native defects and their doping response in the lithium solid electrolyte Li$_7$La$_3$Zr$_2$O$_{12}$, Chem. Mater. **32**, 1876 (2020).

[36] S. Poncé, E. Margine, C. Verdi, and F. Giustino, EPW: Electron-phonon coupling, transport and superconducting properties using maximally localized Wannier functions, Comput. Phys. Commun. **209**, 116 (2016).

[37] S. Poncé, D. Jena, and F. Giustino, Hole mobility of strained GaN from first principles, Phys. Rev. B **100**, 085204 (2019).

[38] S. Poncé, W. Li, S. Reichardt, and F. Giustino, First-principles calculations of charge carrier mobility and conductivity in bulk semiconductors and two-dimensional materials, Rep. Prog. Phys. **83**, 036501 (2020).

[39] J. M. Frost, Calculating polaron mobility in halide perovskites, Phys. Rev. B **96**, 195202 (2017).

[40] A. M. Ganose, J. Park, A. Faghaninia, R. Woods-Robinson, K. A. Persson, and A. Jain, Efficient calculation of carrier scattering rates from first principles, Nat. Commun. **12**, 2222 (2021).

[41] D. O. Scanlon, A. B. Kehoe, G. W. Watson, M. O. Jones, W. I. F. David, D. J. Payne, R. G. Egdell, P. P. Edwards, and A. Walsh, Nature of the band gap and origin of the conductivity of PbO$_2$ revealed by theory and experiment, Phys. Rev. Lett. **107**, 246402 (2011).

[42] D. O. Scanlon, P. D. C. King, R. P. Singh, A. de la Torre, S. M. Walker, G. Balakrishnan, F. Baumberger, and C. R. A. Catlow, Controlling bulk conductivity in topological insulators: Key role of anti-site defects, Adv. Mater. **24**, 2154 (2012).

[43] C. G. Van de Walle, Hydrogen as a Cause of Doping in Zinc Oxide, Phys. Rev. Lett. **85**, 1012 (2000).

[44] A. Squires, J. M. Dean, and B. J. Morgan, Aliovalent doping response and impact on ionic conductivity in the antiperovskite solid electrolyte Li$_3$OCl, ChemRxiv, doi:10.33774/chemrxiv-2021-hzrls.

[45] Z. Zhu, I.-H. Chu, Z. Deng, and S. P. Ong, Role of Na$^+$ interstitials and dopants in enhancing the Na$^+$ conductivity of the cubic Na$_3$PS$_4$ superionic conductor, Chem. Mater. **27**, 8318 (2015).

[46] N. Bernstein, M. D. Johannes, and K. Hoang, Origin of the structural phase transition in Li$_7$La$_3$Zr$_2$O$_{12}$, Phys. Rev. Lett. **109**, 205702 (2012).

[47] T. Fuchs, S. P. Culver, P. Till, and W. G. Zeier, Defect-mediated conductivity enhancements in Na$_{3-x}$Pn$_{1-x}$W$_x$S$_4$ (Pn = P, Sb) using aliovalent substitutions, ACS Energy Lett. **5**, 146 (2020).

[48] C. Kittel, *Thermal Physics* (W. H. Freeman, San Francisco, 1980).

[49] S. B. Zhang and J. E. Northrup, Chemical Potential Dependence of Defect Formation Energies in GaAs: Application to Ga Self-Diffusion, Phys. Rev. Lett. **67**, 2339 (1991).

[50] S. Kim, S. N. Hood, J.-S. Park, L. D. Whalley, and A. Walsh, Quick-start guide for first-principles modelling of point defects in crystalline materials, J. Phys. Energy **2**, 036001 (2020).

[51] C. Franchini, M. Reticcioli, M. Setvin, and U. Diebold, Polarons in materials, Nat. Rev. Mater. **6**, 560 (2021).

[52] R. W. Hellwarth and I. Biaggio, Mobility of an electron in a multimode polar lattice, Phys. Rev. B **60**, 299 (1999).

[53] R. P. Feynman, Slow electrons in a polar crystal, Phys. Rev. **97**, 660 (1955).

[54] See Supplemental Material at http://link.aps.org/supplemental/10.1103/PhysRevMaterials.6.085401 for a comparison of the electronic structure of tetragonal and cubic LLZO, details on modeling polaron properties and defect transition-level diagrams for the chemical potentials defined by the vertices of the syntheically accessible chemical potential stability region for LLZO (Fig. 3). The Supplemental Material also contains Refs. [109–114].

[55] P. Y. Yu and M. Cardona, *Fundamentals of Semiconductors* (Springer, Berlin, 2010).

[56] W. H. Sio, C. Verdi, S. Poncé, and F. Giustino, Polarons from First Principles, without Supercells, Phys. Rev. Lett. **122**, 246403 (2019).

[57] C. Wang, K. Fu, S. P. Kammampata, D. W. McOwen, A. J. Samson, L. Zhang, G. T. Hitz, A. M. Nolan, E. D. Wachsman, Y. Mo, V. Thangadurai, and L. Hu, Garnet-type solid-state electrolytes: Materials, interfaces, and batteries, Chem. Rev. **120**, 4257 (2020).

[58] J. Awaka, A. Takashima, K. Kataoka, N. Kijima, Y. Idemoto, and J. Akimoto, Crystal structure of fast lithium-ion-conducting cubic Li$_7$La$_3$Zr$_2$O$_{12}$, Chem. Lett. **40**, 60 (2011).

[59] J. Awaka, N. Kijima, H. Hayakawa, and J. Akimoto, Synthesis and structure analysis of tetragonal Li$_7$La$_3$Zr$_2$O$_{12}$ with the garnet-related type structure, J. Solid State Chem. **182**, 2046 (2009).

[60] Experimental lattice parameters for c-LLZO and t-LLZO are $a = 12.968$Å for c-LLZO [117] and $a = 13.134$Å, $c = 12.663$Å for t-LLZO [59].

[61] A. G. Squires, D. O. Scanlon, and B. J. Morgan, Dataset for native defects and their doping response in the lithium solid electrolyte Li$_7$La$_3$Zr$_2$O$_{12}$, https://researchdata.bath.ac.uk/691/.

[62] A. G. Squires, supporting code, https://github.com/alexsquires/low_electronic_conductivity_in_LLZO.

[63] https://doi.org/10.15125/BATH-01167.

[64] S. P. Ong, W. D. Richards, A. Jain, G. Hautier, M. Kocher, S. Cholia, D. Gunter, V. L. Chevrier, K. A. Persson, and G. Ceder, Python materials genomics (pymatgen): A robust, open-source python library for materials analysis, Comput. Mater. Sci. **68**, 314 (2013).

[65] J. D. Hunter, Matplotlib: A 2D graphics environment, Comput. Sci. Eng. **9**, 90 (2007).

[66] W. McKinney, Data structures for statistical computing in Python, in *Proceedings of the 9th Python in Science Conference*, edited by S. van der Walt and J. Millman (2010), pp. 56–61.

[67] S. v. d. Walt, S. C. Colbert, and G. Varoquaux, The numpy array: A structure for efficient numerical computation, Comput. Sci. Eng. **13**, 22 (2011).

[68] P. Virtanen, R. Gommers, T. E. Oliphant, M. Haberland, T. Reddy, D. Cournapeau, E. Burovski, P. Peterson, W. Weckesser, J. Bright, S. J. van der Walt, M. Brett, J. Wilson, K. J. Millman, N. Mayorov, A. R. J. Nelson, E. Jones, R. Kern, E. Larson, C. J. Carey *et al.*, SciPy 1.0: fundamental

algorithms for scientific computing in Python, Nat. Methods **17**, 261 (2020).

[69] J. M. Skelton, L. A. Burton, A. J. Jackson, F. Oba, S. C. Parker, and A. Walsh, Lattice dynamics of the tin sulphides SnS_2, SnS and Sn_2S_3: vibrational spectra and thermal transport, Phys. Chem. Chem. Phys. **19**, 12452 (2017).

[70] B. J. Morgan; vasppy: A python suite for manipulating VASP input and output, https://github.com/bjmorgan/vasppy.

[71] C. O. da Costa-Luis, tqdm: A fast, extensible progress meter for Python and CLI, J. Open Source Software **4**, 1277 (2019).

[72] L. D. Whalley, effmass: An effective mass package, J. Open Source Software **3**, 797 (2018).

[73] J. Moore Frost, PolaronMobility.jl: Implementation of the feynman variational polaron model, J. Open Source Software **3**, 566 (2018).

[74] B. J. Morgan and A. G. Squires, py-sc-fermi, https://github.com/bjmorgan/py-sc-fermi.

[75] G. Kresse and J. Hafner, *Ab initio* molecular dynamics for liquid metals, Phys. Rev. B **47**, 558 (1993).

[76] G. Kresse and J. Hafner, *Ab initio* molecular-dynamics simulation of the liquid-metal–amorphous-semiconductor transition in germanium, Phys. Rev. B **49**, 14251 (1994).

[77] G. Kresse and J. Furthmüller, Efficient iterative schemes for ab initio total-energy calculations using a plane-wave basis set, Phys. Rev. B **54**, 11169 (1996).

[78] P. E. Blöchl, Projector augmented-wave method, Phys. Rev. B **50**, 17953 (1994).

[79] J. Heyd, G. E. Scuseria, and M. Ernzerhof, Hybrid functionals based on a screened coulomb potential, J. Chem. Phys. **118**, 8207 (2003).

[80] A. V. Krukau, O. A. Vydrov, A. F. Izmaylov, and G. E. Scuseria, Influence of the exchange screening parameter on the performance of screened hybrid functionals, J. Chem. Phys. **125**, 224106 (2006).

[81] F. D. Murnaghan, The compressibility of media under extreme pressures, Proc. Natl. Acad. Sci. USA **30**, 244 (1944).

[82] M. Gajdoš, K. Hummer, G. Kresse, J. Furthmüller, and F. Bechstedt, Linear optical properties in the projector-augmented wave methodology, Phys. Rev. B **73**, 045112 (2006).

[83] J. P. Perdew, A. Ruzsinszky, G. I. Csonka, O. A. Vydrov, G. E. Scuseria, L. A. Constantin, X. Zhou, and K. Burke, Restoring the Density-Gradient Expansion for Exchange in Solids and Surfaces, Phys. Rev. Lett. **100**, 136406 (2008).

[84] S. Lany and A. Zunger, Assessment of correction methods for the band-gap problem and for finite-size effects in supercell defect calculations: Case studies for ZnO and GaAs, Phys. Rev. B **78**, 235104 (2008).

[85] S. T. Murphy and N. D. M. Hine, Anisotropic charge screening and supercell size convergence of defect formation energies, Phys. Rev. B **87**, 094111 (2013).

[86] J. Yan, P. Gorai, B. Ortiz, S. Miller, S. A. Barnett, T. Mason, V. Stevanović, and E. S. Toberer, Material descriptors for predicting thermoelectric performance, Energy Environ. Sci. **8**, 983 (2015).

[87] J. E. N. Swallow, B. A. D. Williamson, S. Sathasivam, M. Birkett, T. J. Featherstone, P. A. E. Murgatroyd, H. J. Edwards, Z. W. Lebens-Higgins, D. A. Duncan, M. Farnworth, P. Warren, N. Peng, T.-L. Lee, L. F. J. Piper, A. Regoutz, C. J. Carmalt, I. P. Parkin, V. R. Dhanak, D. O. Scanlon,

and T. D. Veal, Resonant doping for high mobility transparent conductors: the case of Mo-doped In_2O_3, Mater. Horiz. **7**, 236 (2020).

[88] L. D. Whalley, J. M. Frost, B. J. Morgan, and A. Walsh, Impact of nonparabolic electronic band structure on the optical and transport properties of photovoltaic materials, Phys. Rev. B **99**, 085207 (2019).

[89] For comparison, the charge-carrier effective masses in semiconductors being investigated or used as photovoltaics, which rely on mobile electronic charge carriers, (e.g., $CH_3NH_3PbI_3$ or Cu_2ZnSnS_4) are typically <1 [88].

[90] For comparison, carrier mobilities in doped indium oxides used as in commercial devices as transparent conducting oxides are of the order 10 to 100 cm^2 $V^{-1}s$ [87].

[91] C. J. Bradley, *The Mathematical Theory of Symmetry in Solids: Representation Theory for Point Groups and Space Groups* (Clarendon Press, Oxford, 2010).

[92] P. Canepa, J. A. Dawson, G. S. Gautam, J. M. Statham, S. C. Parker, and M. S. Islam, Particle morphology and lithium segregation to surfaces of the $Li_7La_3Zr_2O_{12}$ solid electrolyte, Chem. Mater. **30**, 3019 (2018).

[93] CRC Handbook, *CRC Handbook of Chemistry and Physics*, 88th ed. (CRC Press, Boca Raton, FL, 2007).

[94] M. Finnis, A. Lozovoi, and A. Alavi, The oxidation of NiAl: What can we learn from ab initio calculations?, Annu. Rev. Mater. Res. **35**, 167 (2005).

[95] V. Thangadurai, S. Narayanan, and D. Pinzaru, Garnet-type solid-state fast Li ion conductors for Li batteries: critical review, Chem. Soc. Rev. **43**, 4714 (2014).

[96] K. Sasaki and J. Maier, Low-temperature defect chemistry of oxides. I. General aspects and numerical calculations, J. Appl. Phys. **86**, 5422 (1999).

[97] J. Maier, Complex oxides: High temperature defect chemistry vs. low temperature defect chemistry, Phys. Chem. Chem. Phys. **5**, 2164 (2003).

[98] R. Brugge, J. Kilner, and A. Aguadero, Germanium as a donor dopant in garnet electrolytes, Solid State Ionics **337**, 154 (2019).

[99] F. Pesci, R. H. Brugge, A. K. O. Hekselman, A. Cavallaro, R. J. Chater, and A. Aguadero, Elucidating the role of dopants in the critical current density for dendrite formation in garnet electrolytes, J. Mater. Chem. A **6**, 19817 (2018).

[100] E. Rangasamy, J. Wolfenstine, and J. Sakamoto, The role of Al and Li concentration on the formation of cubic garnet solid electrolyte of nominal composition $Li_7La_3Zr_2O_{12}$, Solid State Ionics **206**, 28 (2012).

[101] T. Thompson, S. Yu, L. Williams, R. D. Schmidt, R. Garcia-Mendez, J. Wolfenstine, J. L. Allen, E. Kioupakis, D. J. Siegel, and J. Sakamoto, Electrochemical window of the Li-ion solid electrolyte $Li_7La_3Zr_2O_{12}$, ACS Energy Lett. **2**, 462 (2017).

[102] M. Yi, T. Liu, X. Wang, J. Li, C. Wang, and Y. Mo, High densification and Li-ion conductivity of Al-free $Li_{7-x}La_3Zr_{2-x}TaO_{12}$ garnet solid electrolyte prepared by using ultrafine powders, Ceram. Int. **45**, 786 (2019).

[103] Our model assumes that electronic carrier populations formed through thermal excitation at high temperature—e.g., directly after synthesis—re-equilibrate on experimental timescales. If some proportion of electronic carriers however *do not* re-equilibrate during cooling, this would give considerably higher room-temperature carrier concentrations, and higher

electronic conductivities, than predicted by our pseudoequilibrium model, although this behaviour would require some mechanism for trapping "hot" electronic carriers on experimentally relevant timescales.

[104] X. Liu, R. Garcia-Mendez, A. R. Lupini, Y. Cheng, Z. D. Hood, F. Han, A. Sharafi, J. C. Idrobo, N. J. Dudney, C. Wang, C. Ma, J. Sakamoto, and M. Chi, Local electronic structure variation resulting in Li 'filament' formation within solid electrolytes, Nat. Mater. **20**, 1485 (2021).

[105] J. M. Dean, S. W. Coles, W. R. Saunders, A. R. McCluskey, M. J. Wolf, A. B. Walker, and B. J. Morgan, Overscreening and Underscreening in Solid-Electrolyte Grain Boundary Space-Charge Layers, Phys. Rev. Lett. **127**, 135502 (2021).

[106] Y. Aizawa, K. Yamamoto, T. Sato, H. Murata, R. Yoshida, C. A. Fisher, T. Kato, Y. Iriyama, and T. Hirayama, In situ electron holography of electric potentials inside a solid-state electrolyte: Effect of electric-field leakage, Ultramicroscopy **178**, 20 (2017).

[107] M. W. Swift, J. W. Swift, and Y. Qi, Modeling the electrical double layer at solid-state electrochemical interfaces, Nat. Comput. Sci. **1**, 212 (2021).

[108] M. Smeu and K. Leung, Electron leakage through heterogeneous LiF on lithium-metal battery anodes, Phys. Chem. Chem. Phys. **23**, 3214 (2021).

[109] B. Guster, P. Melo, B. A. A. Martin, V. Brousseau-Couture, J. C. de Abreu, A. Miglio, M. Giantomassi, M. Côté, J. M. Frost, M. J. Verstraete, and X. Gonze, Fröhlich polaron effective mass and localization length in cubic materials: Degenerate and anisotropic electronic bands, Phys. Rev. B **104**, 235123 (2021).

[110] D. W. Davies, C. N. Savory, J. M. Frost, D. O. Scanlon, B. J. Morgan, and A. Walsh, Descriptors for electron and hole charge carriers in metal oxides, J. Phys. Chem. Lett. **11**, 438 (2020).

[111] J. Sjakste, N. Vast, M. Calandra, and F. Mauri, Wannier interpolation of the electron-phonon matrix elements in polar semiconductors: Polar-optical coupling in GaAs, Phys. Rev. B: Condens. Matter **92**, 054307 (2015).

[112] C. Verdi and F. Giustino, Fröhlich Electron-Phonon Vertex from First Principles, Phys. Rev. Lett. **115**, 176401 (2015).

[113] Y. Ōsaka, Polaron state at a finite temperature, Prog. Theor. Phys. **22**, 437 (1959).

[114] T. D. Schultz, Slow electrons in polar crystals: Self-Energy, mass, and mobility, Phys. Rev. **116**, 526 (1959).

[115] L. C. D. Jonghe, L. Feldman, and A. Buechele, Failure modes of Na-beta alumina, Solid State Ionics **5**, 267 (1981).

[116] L. C. D. Jonghe, L. Feldman, and A. Beuchele, Slow degradation and electron conduction in sodium/beta-aluminas, J. Mater. Sci. **16**, 780 (1981).

[117] R. Murugan, V. Thangadurai, and W. Weppner, Fast lithium ion conduction in garnet-type $Li_7La_3Zr_2O_{12}$, Angew. Chem. Int. Ed. **46**, 7778 (2007).

[118] http://www.archer.ac.uk.